Chinese Chemical Letters 34 (2023) 108584

Contents lists available at ScienceDirect

Chinese Chemical Letters

journal homepage: www.elsevier.com/locate/cclet

# Nano-silver-modified polyphosphazene nanoparticles with different morphologies: Design, synthesis, and evaluation of antibacterial activity

Tairong Kuang[a], Linbing Deng[a], Sitao Shen[a], Hongxia Deng[b], Zhisen Shen[b,*], Zhenjie Liu[c,*], Zhengping Zhao[a], Feng Chen[a], Mingqiang Zhong[a]

[a] Zhejiang Key Laboratory of Plastic Modification and Processing Technology, College of Material Science and Engineering, Zhejiang University of Technology, Hangzhou 310014, China
[b] Department of Otorhinolaryngology, Head and Neck Surgery, The Affiliated LiHuili Hospital, Ningbo University, Ningbo 315040, China
[c] Department of Vascular Surgery, Second Affiliated Hospital of Zhejiang University School of Medicine, Hangzhou 310009, China

ARTICLE INFO

*Article history:*
Received 3 April 2023
Revised 15 May 2023
Accepted 16 May 2023
Available online 21 May 2023

*Keywords:*
Nano-silver
Polyphosphazene
Morphology change
Antibacterial activity
Antibacterial mechanism

ABSTRACT

Drug-resistant bacteria present a severe threat to public health, emphasizing the importance of developing broad-spectrum antibacterial agents that are free from drug resistance. Among silver-based antibacterial agents, nano-silver has been found to exhibit the most promising and comprehensive performance. The exploration of the antibacterial capacity and morphological changes of silver nanoparticles (AgNPs) could offer a starting point for the development of safe and efficient antibacterial agents. In this study, three types of nano-silver-modified polyphosphazene (PRV) nanoparticles with different morphologies were synthesized using precipitation polymerization. These nanoparticles were characterized using various techniques, including Fourier-transform infrared spectroscopy (FTIR), X-ray diffraction (XRD), scanning electron microscopy (SEM), transmission electron microscopy (TEM), and thermogravimetric analysis (TGA). The antibacterial activity of these nanoparticles against *Escherichia coli* (*E. coli*) and *Staphylococcus aureus* (*S. aureus*) was assessed using minimum inhibitory concentration (MIC)/minimum bactericidal concentration (MBC) tests and inverted fluorescence microscopy. Our results revealed that the antibacterial activity of silver nanoparticles can vary significantly depending on their immobilized form. Ag@PRV Strawberry-like nanoparticles (NPs) exhibited higher antibacterial activity compared to Ag@PRV Yolk-Shell NPs and Ag@PRV Cable-like nanofibers (NFs). Notably, all three types of synthesized nanoparticles demonstrated a stronger bactericidal effect on Gram-positive bacteria than Gram-negative bacteria. Live/dead bacterial staining and scanning electron microscopy demonstrated that silver can kill bacteria by altering the permeability of their cell membranes. These findings offer valuable insights for designing and practically applying new silver-based antibacterial agents in the future.



Silver has been widely used as an antibacterial agent for many years, and its potential practical applications have gained substantial momentum in various fields, including public health, biomedical and food safety [1]. The corona virus disease 2019 (COVID-19) pandemic and the emergence of super-resistant bacteria have further accelerated interest in silver-based solutions. While conventional silver-based products such as implants, bandages, gels, and surgical wires have been in use, recent years have witnessed the development of several new silver-containing products, particularly nano-silver products [2–5].

There is a growing consensus that reducing the size of materials to the nanoscale can enhance their commercial value, enabling them to perform novel and superior functions [6–8]. For instance, macro-scale silver can be converted into nanoparticles (NPs) with significantly improved antibacterial properties, exhibiting broad-spectrum sterilization without drug resistance. Furthermore, studies indicate that silver can promote wound healing, making it a focal point of medical research [2,9]. However, silver nanoparticles (AgNPs) have limitations, including agglomeration, biotoxicity, easy oxidation, and bioaccumulation [10,11]. To address these issues, doping or adding AgNPs to various matrices has been proposed as a potential solution. For instance, Vijaya *et al.* developed a novel nanocomposite with improved antibacterial properties by embed-

* Corresponding authors.
*E-mail addresses:* szs7216@163.com (Z. Shen), lawson4001@zju.edu.cn (Z. Liu).

https://doi.org/10.1016/j.cclet.2023.108584
1001-8417/

ding AgNPs into graphene oxide cellulose, mediated by catechin (CA) [12]. Ge *et al.* employed a simple one-step procedure utilizing crab shells to prepare iminodisuccinate (IDS)-modified chitin for adsorbing Ag. This research not only attained enhanced antibacterial properties but also successfully accomplished various objectives such as waste utilization, resource recovery, and reutilization [13]. Additionally, Xu *et al.* developed a novel material, consisting of calcium alginate gels-functionalized polyurethane form (PUF) decorated with AgNPs, that showed excellent long-term antibacterial activity [14]. Therefore, the identification of suitable carrier materials to loaded silver antibacterial agents remains an important task for improving the dispersibility, stability, and safety of AgNPs [15–22].

Polymeric nanocarriers have become increasingly popular in recent years for delivering drugs to improve the efficacy of chemotherapeutics, such as NSC23766 [23], STM@8P4 [24], and doxorubicin (DOX) [25]. These drugs are loaded into phenylalanine-based poly(ester amide) (Phe-PEA) NPs, which offer several advantages over traditional carriers. NP systems are known to effectively reduce biotoxicity levels, improve drug transport efficiency, and provide sustained drug release. Polyphosphazene, a type of organic-inorganic hybrid polymer, is characterized by an alternating arrangement of nitrogen and phosphorus elements in its main chain, and organic substituents in its side chain. It boasts of several attractive features, such as high or low-temperature resistance, organic solvent resistance, excellent molecular designability, and good biocompatibility than Phe-PEA NPs. In our previous study [26], we reported that a poly(cyclotriphos-phonitrile-*co*-3,4′,5-trihydroxystilbene) material (PRV) obtained through the precipitation polymerization of hexachlorocyclophosphazene and resveratrol exhibited high bactericidal activity and low toxicity upon combining with Ag ions. Furthermore, the surface of the PRV contains abundant active functional groups that capture silver ions and act as reaction sites, thus simplifying the preparation process. Compared to ionic silver, the biological toxicity of silver NPs is much lower at the same molar concentration. Thus, combining PRV with AgNPs has great potential for addressing the drawbacks of nano silver application.

In this study, we developed and synthesized three distinct shapes and structures of nano-silver-modified PRV NPs, including Ag@PRV Cable-like nanofibers (NFs), Ag@PRV Yolk-Shell NPs, and Ag@PRV Strawberry-like NPs. The precipitation polymerization of hexachlorocyclophosphazene and resveratrol yielded PRV, which was then bound with nano-silver in the form of a hard template or secondary reduction. The synthesis of PRV was facilitated using ultrasound, and the surface functional groups of PRV served as anchor sites for silver ions and nano-silver through electrostatic interactions, resulting in a green, mild, safe, and straightforward preparation process. The morphology and structure of Ag@PRV NPs were systematically analyzed, and comparative analysis was used to explore differences in their antibacterial properties. Furthermore, we investigated the anti-bactericidal mechanism of the antibacterial agents on various bacteria groups using electron microscopy and inverted fluorescence microscopy, revealing the mechanisms underlying the difference in bactericidal effects.

In prior research [26], the combination of silver nitrate and PRV NPs displayed robust bactericidal effects through silver ions and biological effects *via* the resveratrol backbone. The composite exhibited excellent antibacterial properties and significantly decreased cytotoxicity at optimal concentrations. Furthermore, the composite stimulated the activation of mouse fibroblasts, indicating a promising application. Based on these results, we continued to use PRV materials. It has been established that the unique properties of NPs are closely linked to their morphology. The regulation of nanoparticle morphology can be achieved by changing experimental conditions such as influencing the stabilization factors in the synthesis process or adding exotic templates [27]. Tang *et al.* have explored a variety of cyclic cross-linked polyphosphazene with unique molecular structures and morphologies [28–31], such as nanofibers, nanotubes, nanospheres, hollow spheres, layered structures, and others, all of which exhibit significant research value.

The present study describes the schematic synthesis of three distinct nano-silver-modified polyphosphazene (PRV) NPs: Ag@PRV Strawberry-like NPs, Ag@PRV Yolk-Shell NPs, and Ag@PRV Cable-like NFs, under various reaction conditions, as depicted in Fig. 1. The synthesis of PRV NPs follows the typical oligomer adsorption mechanism [32]. As shown in Fig. S1 (Supporting information), the precipitation polymerization of resveratrol (RSV) and hexachlorocyclotriphosphazene (HCCP) was conducted using acetonitrile as a solvent and excess triethylamine (TEA) as an acid-binding agent to provide energy through ultrasonication. Initially, HCCP reacts with RSV to form hydrogen chloride (HCl), which is captured by TEA to form triethylamine hydrochloride crystals. This, in turn, promotes nucleophilic substitution between the hydroxyl (-OH) terminal of RSV and the P-Cl functional group in HCCP. The specific shape of PRV particles can be prepared by inducing precipitation and polymerization with a hard template during the early stage of the reaction. Although hard templates are introduced in the synthesis of both Ag@PRV Cable-like NFs and Ag@PRV Yolk-Shell NPs, Ag@PRV Cable-like nanofibers require lower ultrasonic power during the reaction to maintain stability. Strong external disturbance can destroy the stability of the deposition, leading to the self-assembly of PRV and growth of spherical NPs. In addition, the synthesis process of Ag@PRV Strawberry-like NPs involves surface modification of PRV NPs and secondary growth of silver to ensure uniform adsorption of $Ag^{+}$ on the surface of the nanosphere through electrostatic interactions, followed by *in situ* reduction to silver NPs to obtain the final strawberry structure. *In situ* reduction of PRV directly in silver nitrate solution resulted in unsatisfactory outcomes due to self-agglomeration or agglomeration of silver NPs on the surface of PRV (Fig. S2 in Supporting information). Therefore, modification of the surface potential by PEI was necessary to achieve the desired structure [33–36]. The specific synthesis processes are described in Supporting information.

The present study focuses on examining the encapsulation process of nano-silver-modified PRV NPs and exploring the bonding mechanism between primary NPs and the hard template. The scanning electron microscopy (SEM) and transmission electron microscopy (TEM) were utilized to examine the morphology of the three PRV NPs loaded with silver (Ag@PRV Cable-like NFs, Ag@PRV Yolk-Shell NPs, and Ag@PRV Strawberry-like NPs) (for a detailed description of all the test procedure, please refer to the Supporting information). The SEM and TEM images presented in Figs. 2a and b demonstrated that the Ag@PRV Yolk-Shell NPs exhibited uniform particle size and a certain roughness on the surface, which was attributed to the pores in the shell. The diameter of the nanospheres ranged from 500 nm to 700 nm, and they exhibited good dispersion with no adhesion. Furthermore, the nano-silver was successfully encapsulated in the PRV particles with uniform distribution, displaying a unique yolk-egg-shell structure with a shell layer thickness of approximately 250–300 nm and a nano-silver core with a particle size ranging from 100 nm to 200 nm.

Figs. 2c and d show the TEM images of Ag@PRV Strawberry-like NPs, which exhibit uniform coverage of AgNPs with a size range of 20–40 nm on the PRV spheres, preventing self-agglomeration outside the spheres. The trace AgNPs initially formed on the PEI-PRV surface underwent secondary growth to achieve the desired effect, as observed. Upon changing the hard template from AgNPs to AgNFs, ultrasonic radiation supplied the necessary energy for the primary NPs to aggregate and deposit around the Ag nanowires. This process ultimately resulted in the formation of cable-like core-shell NPs with a silver core and PRV shell. The key to this process was

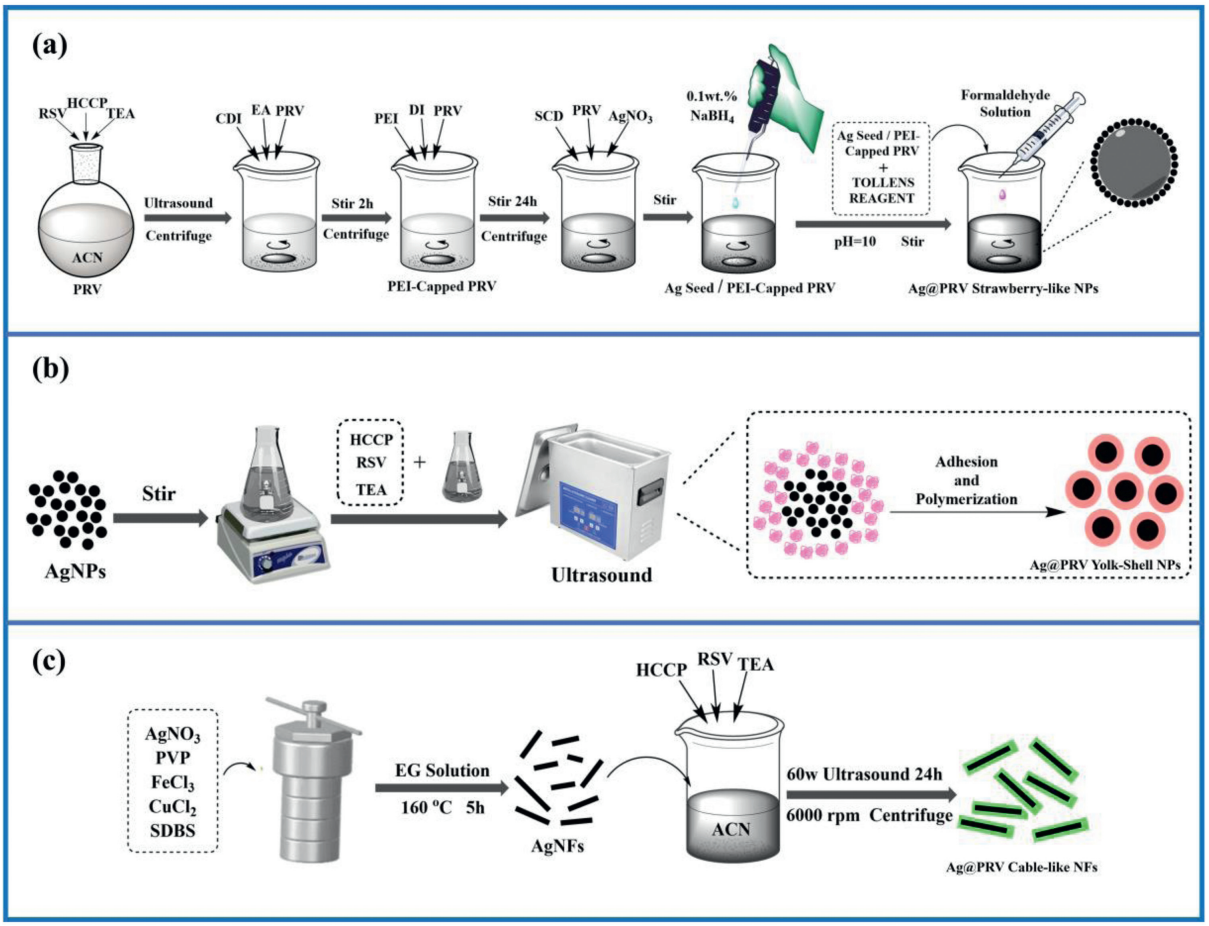


**Fig. 1.** Schematic illustration of the synthetic procedure for nano-silver-modified PRV NPs with different morphologies: (a) Ag@PRV Strawberry-like NPs, (b) Ag@PRV Yolk-Shell NPs, and (c) Ag@PRV Cable-like NFs.

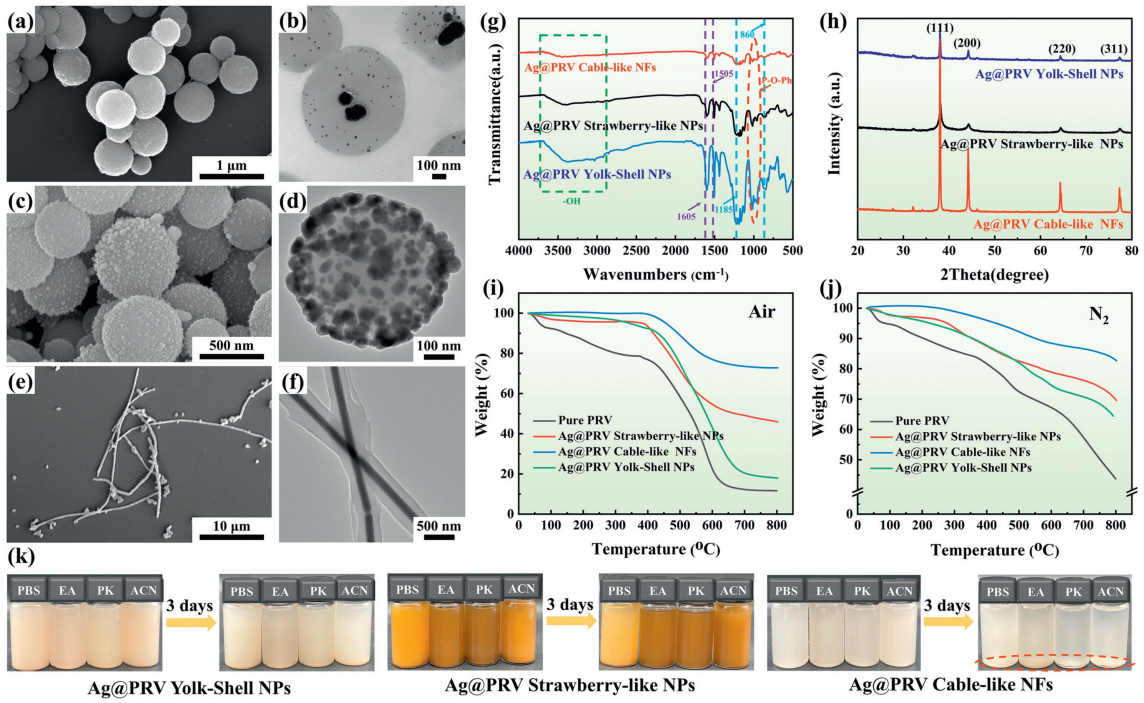


**Fig. 2.** Characterization of nano-silver-modified PRV NPs with different morphologies: (a–f) SEM and TEM images; (g) FT-IR spectra; (h) XRD patterns; (i, j) thermogravimetric analysis (TGA) results performed under $N_2$ or air atmosphere at a heating rate of 10 °C/min; (k) photographs of Ag@PRV NPs dispersed in different solvents, including phosphate buffered saline (PBS), ethanol (EA), acetone (PK), and acetonitrile (ACN).

ultrasonic treatment, as an excessively strong external perturbation could destabilize the deposition and lead to the growth of PRV into spherical particles without template self-assembly. As shown in Figs. 2e and f, the diameter of the coaxial cable was about 300–400 nm, while the diameter of the internal silver nanowires was about 140 nm, and the PRV was successfully deposited wrapped on the surface of the nanowires. As depicted in Fig. 2g, the absorption peak observed at 960 $cm^{-1}$ in the FTIR spectrum was assigned to P-O-(Ph), which provided strong evidence for the polycondensation cross-linking between HCCP and RSV. Fig. 2h displays the XRD diffraction patterns of the three materials. The diffraction peaks observed at 38°, 44°, 64°, and 77° correspond to the characteristic peaks of Ag(111), Ag(200), Ag(220), and Ag(311), respectively. The presence of these absorption peaks in the FTIR and diffraction characteristic peaks in the XRD spectra confirmed the synthesis of PRV and the successful loading of silver. As shown in Fig. 2i, thermogravimetric analysis (TGA) showed that the Ag@PRV Yolk-Shell NPs carried 6.3 wt% silver, Ag@PRV Strawberry-like NPs 34.2 wt% silver, and Ag@PRV Cable-like NFs up to 61.1 wt% silver. The silver loading of the other two PRV nanomaterials was significantly higher than previously reported in the literature [37,38], except for the Ag@PRV Yolk-Shell NPs. The thermal stability of the nanoparticle was measured using TGA in a nitrogen atmosphere, and the thermal weight loss curves of all three materials became flat when the PRV materials were loaded with silver (Fig. 2j). The physical resistance effect brought by the introduction of silver could also enhance the thermal stability of the system, and the higher the silver content, the flatter the curve. The weight loss process could be divided into three stages, with the initial weight loss caused by the escape of gas from the porous shell layer of the material, the disintegration of the phosphonitrile ring in the intermediate stage, and the destruction of the phosphonitrile ring's structure, leading to the release of nitrogen as $N_2$ and the sublimation of phosphorus. White phosphorus was also transformed into red phosphorus at this temperature [39]. Observations were made regarding the thermal weight loss curves of the three materials loaded with silver, specifically that the curves flattened as the silver content increased. This implies that the physical resistance effect induced by the introduction of silver can enhance the thermal stability of the system [40].

Polyphosphazene carriers containing multiple hydroxyl groups have been demonstrated to prevent nanoparticle agglomeration by enhancing dispersion and stability in solution systems through spatial effects and surface potential. To investigate this phenomenon, we subjected three nano-silver-modified PRV NPs to sonication in various solvent systems, including phosphate buffered saline (PBS), ethanol (EA), acetone (PK), and acetonitrile (ACN), and subsequently monitored sedimentation. The results, as depicted in Fig. 2k, indicated that all NPs were evenly dispersed in both aqueous and organic phases after sonication. However, the sedimentation phenomenon was observed for Ag@PRV Cable-like NFs after three days, potentially due to the wire-like nano cables losing their nanoscale properties by entangling with one another.

Pure PRV primarily inhibits silver cytotoxicity while having little impact on antibacterial activity. In our previous study, the antibacterial properties of the composite are mainly determined by the silver ion content. However, the biocidal activity of nano-silver differs from that of free silver ions, and the particle's geometrical factors, such as particle size and surface morphology, play an important role. To further examine the surface elemental composition of the nano-silver-modified PRV NPs, X-ray photoelectron spectroscopy (XPS) was used. The XPS spectra of the three nano-silver-modified PRV NPs and the narrow sweep spectra of the surface Ag elements are shown in Fig. S3 (Supporting information). The specific surface element concentrations are shown in Table S1 (Supporting information). It was found that the surface of the polyphosphononitrile of the shell layer contained a high content of C, O, N, and P elements. The quantification results of Ag content on the surface of the three NPs were inconsistent with the thermogravimetric results, with Ag@PRV Strawberry-like NPs having the highest Ag content on the surface, while Ag@PRV Cable-like NFs and Ag@PRV Yolk-Shell NPs had almost no Ag on the surface. The bactericidal properties of silver NPs have been shown to be subject to the dual synergistic effects of contact bactericidal and silver ion solubilization. The concentration of Ag elements on the surface of the particles is considered to have a significant impact on the subsequent antibacterial effect. The high content of O elements on the surface of the shell layer confirms that the surface of the nanospheres is rich in hydroxyl groups, which contributes to the particles' hydrophilicity and could potentially be used for specific functional modification. Following the observation of variations in the silver loading and surface silver content of the three nano-silver-modified PRV NPs, we proceeded to assess the overall antibacterial efficacy of the different morphologies against two bacterial strains, namely Gram-negative *Escherichia coli* (*E. coli*) and Gram-positive *Staphylococcus aureus* (*S. aureus*).

The antibacterial efficiency of three different nano-silver-modified PRV NPs was evaluated by determining their minimum inhibitory concentration (MIC) and minimum bactericidal concentration (MBC) values against *E. coli* and *S. aureus*. Figs. 3a–d illustrates that Ag@PRV Strawberry-like NPs exhibited the lowest nanoparticle concentration required for clear bacterial suspensions compared to the other two materials. Specifically, the MIC and MBC values for *E. coli* were 39.4 and 156.3 μg/mL, respectively, while the corresponding values for *S. aureus* were 312.5 and 625.0 μg/mL. Conversely, Ag@PRV Cable-like NFs demonstrated good antibacterial activity, with *E. coli* MIC and MBC values of 153.6 and 1250.0 μg/mL, respectively, and *S. aureus* MIC and MBC values of 625.0 and 2500.0 μg/mL, respectively (Table S2 in Supporting information). In contrast, Ag@PRV Yolk-Shell NPs exhibited the lowest antibacterial properties, with *E. coli* MIC and MBC values of 625.0 and 5000 μg/mL, respectively, and *S. aureus* MIC and MBC values of 1250.0 and 10,000.0 μg/mL, respectively.

The determination of specific bactericidal rates of three distinct materials was carried out by bacterial fluorescence imaging analysis. Fluorescence microscopy images of the bacterial suspensions following the exposure of different NPs to the target bacterial solution were obtained and are presented in Fig. 3e. In these images, surviving bacteria appeared green, while dead bacteria appeared red. The physical state and number of bacterial cells were observed to significantly differ among the three materials. The quantitative analysis data of Fig. 3f corroborated the results of MIC and MBC. The highest bactericidal ability was observed for Ag@PRV Strawberry-like NPs, with an *E. coli* killing efficiency rate of approximately 93% and a *S. aureus* killing efficiency rate of approximately 92%. The Ag@PRV Cable-like NFs followed closely, with an *E. coli* killing efficiency rate of approximately 79% and a *S. aureus* survival rate of approximately 70%. Finally, the Ag@PRV Yolk-Shell NPs showed the lowest bactericidal activity with an *E. coli* survival rate of approximately 71% and a *S. aureus* survival rate of approximately 61%.

The antibacterial mechanisms of the three NPs are closely related. Previous studies have shown that nano-silver possesses broad-spectrum bactericidal properties through a dual synergistic effect of nano-silver contact bactericidal action and silver ion solubilization bactericidal action. Nano-silver particles with a high surface potential are known to accumulate on the bacterial surface. Additionally, silver ions released from nano-silver can bind to sulfur-containing proteins and DNA in bacteria, inhibiting DNA translation and transcription and resulting in the release of reactive oxygen species, which affect the normal physiological activities of bacteria [41,42]. In the case of Ag@PRV Cable-like NFs and Ag@PRV

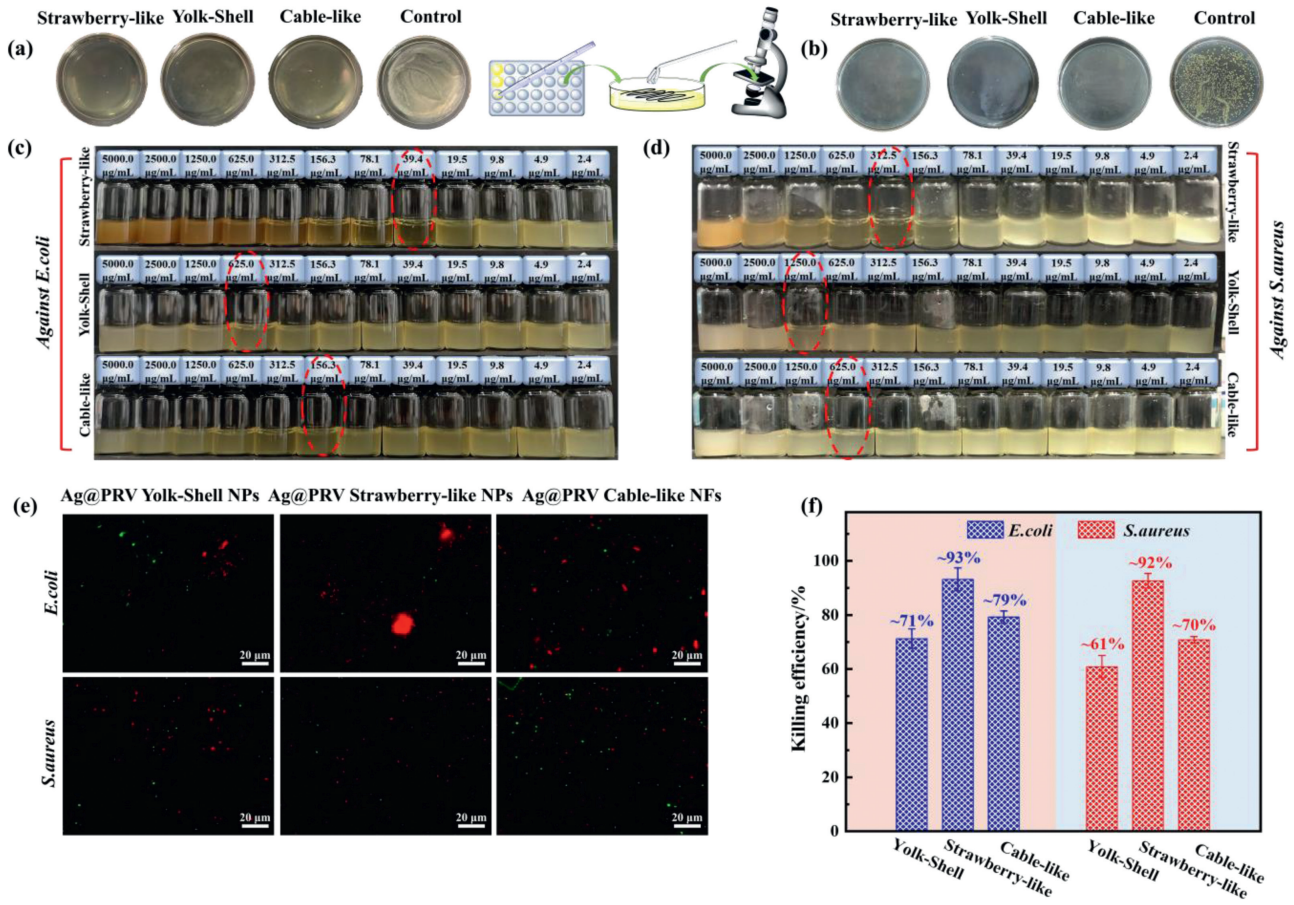


**Fig. 3.** Antibacterial activity of nano-silver-modified PRV NPs with different morphologies against *E. coli* and *S. aureus*: (a, b) CFU counting images of MBC for both bacterial strains; (c, d) MIC test results of different concentrations of NPs; (e) fluorescence microscopy images; (f) killing efficiency ratio.

Yolk-Shell NPs, the polyphosphazene shell layer encapsulates nano-silver, thereby improving its safety. However, nano-silver in these NPs cannot directly contact bacteria and relies on the leaching of silver ions for sterilization. The thickness and composition of the shell layer play a crucial role in the sterilization rate. Ag@PRV Cable-like NFs tend to lose their nano properties due to mutual entanglement, while Ag@PRV Yolk-Shell NPs exhibit poorantibacterial properties due to their low nano-silver content and thick shell layer, which inhibits silver ion diffusion. On the other hand, Ag@PRV strawberry-like NPs have a uniform distribution of silver ions throughout the shell layer, which allows for faster dispersion and direct contact with bacteria. The unrestricted release of silver ions from the shell layer allows for the most effective sterilization through a combination of silver contact sterilization and silver ion dissolution sterilization. While Ag@PRV Cable-like NFs and Ag@PRV Yolk-Shell NPs show relatively lower antibacterial performance, they are still valuable in situations where low toxicity and long-lasting antibacterial effects are desired.

In the antibacterial tests, we observed varying levels of resistance of *E. coli* and *S. aureus* to nano-silver-modified PRV NPs with different morphologies. Interestingly, the material exhibited a stronger selective killing effect on *E. coli* than on *S. aureus*, which may be attributed to the differences in the cell membrane structures of Gram-positive and negative bacteria. As depicted in Fig. 4a, the cell wall of Gram-negative bacteria is more complex, consisting of the outer membrane, peptidoglycan layer, wall membrane gap, and cytoplasmic membrane, whereas the peptidoglycan layer of the cell wall in Gram-positive bacteria is thick and compact in structure. However, the peptidoglycan layer in Gram-negative bacteria is thin, with low peptidoglycan content and a loose structure, rendering them more susceptible to nano-silver-induced membrane damage and death. Conversely, the thick and compact structure of the peptidoglycan layer in Gram-positive bacteria makes it challenging for nano-silver and silver ions to penetrate and alter the membrane permeability [43,44]. To validate this hypothesis, we performed live-dead bacterial staining, fixed the co-cultured bacteria by dehydration and investigated the morphological changes of the bacteria *via* SEM. As illustrated in Figs. 4b, c and h, *E. coli* started to die at 4 h, and almost all *E. coli* in the field of view were dead after 12 h, whereas the death of *S. aureus* increased slowly after 8 h, and almost all *S. aureus* were killed by Ag@PRV Strawberry-like NPs after 12 h, indicating a considerably slower process than that observed for *E. coli*.

Upon examination of SEM images, it was found that *E. coli* cells co-cultured with Ag@PRV Strawberry-like NPs exhibited extensive deformation, and even showed cytoplasmic efflux, as evidenced by Figs. 4d–g [45]. In contrast, while the morphology of *S. aureus* cells was also somewhat distorted, their overall structure remained largely intact, with only slight puckering and no intracellular leakage. Control group bacteria were cultured for 24 h under antibacterial-free conditions and subjected to the same dehydration and fixation procedures. As can be seen from the SEM images, both control group bacterial cells were plump, with smooth surfaces and intact structures. Obviously, the thick chitosan layer effectively hindered the entry of $Ag^{+}$ ions, resulting in a better isolation effect, which helped Gram-positive bacteria to maintain their cellular morphology.

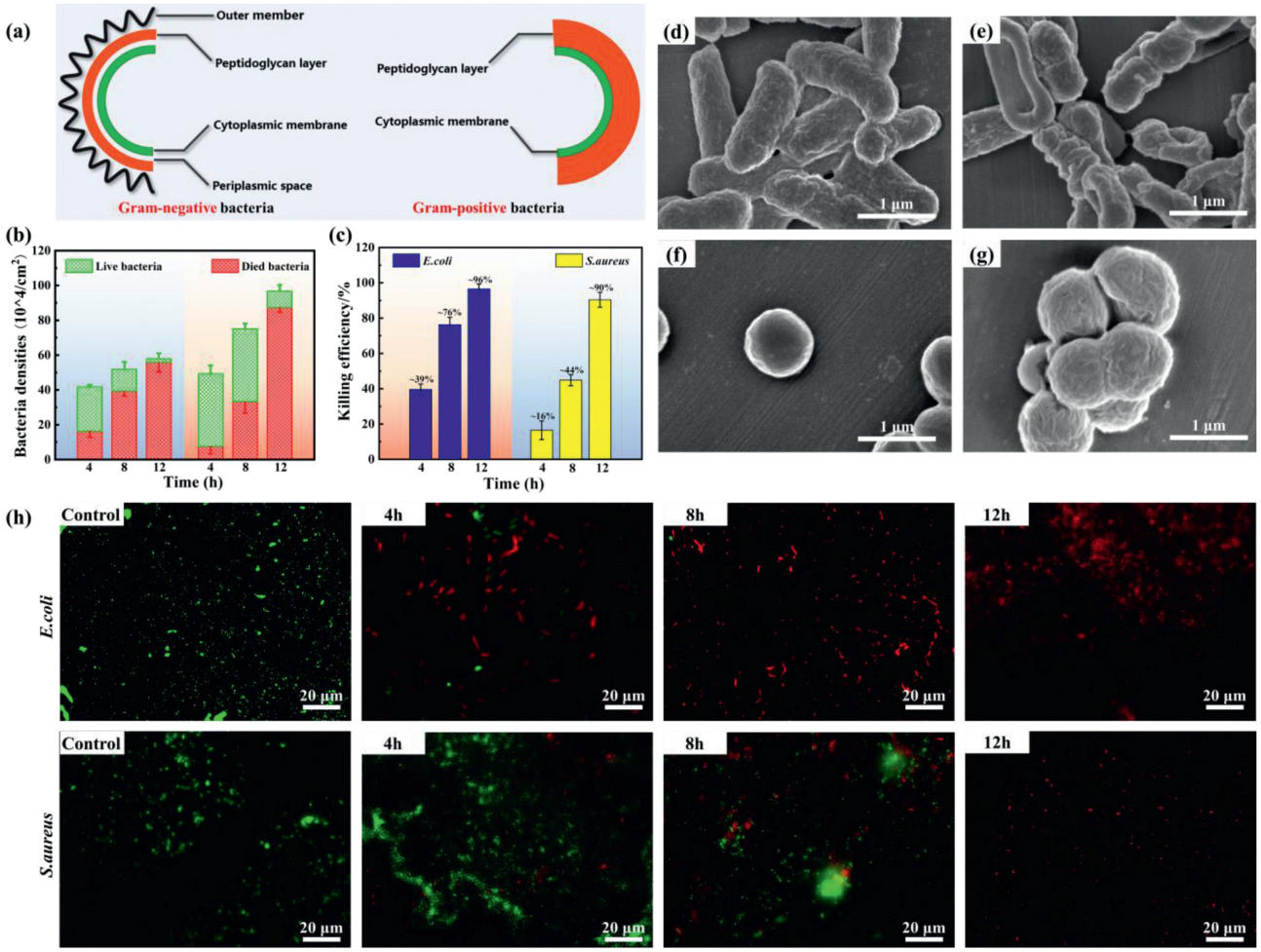


**Fig. 4.** Characterization of nano-silver-modified PRV NPs' antibacterial mechanism: (a) schematic representation of the cell membrane structure of Gram-positive and Gram-negative bacteria; (b) quantitative statistics of *E.coli* and *S.aureus*; (c) killing efficiency ratio of different Ag@PRV NPs against the two bacterial strains; (d–g) SEM images showing the morphological changes of bacteria before and after exposure to Ag@PRV NPs; (h) fluorescence microscopy images demonstrating changes in membrane permeability after treatment with Ag@PRV NPs.

In this study, we designed and prepared three different structures of nano-silver-modified PRV NPs by changing the reaction conditions. The resulting Ag@PRV with different morphologies showed excellent thermal stability, solvent dispersion, and solvent resistance. The silver loading amounts of the three antibacterial agents were determined to be 6.3 wt% for Ag@PRV Yolk-Shell NPs, 34.2 wt% for Ag@PRV Strawberry-like NPs, and 61.1 wt% for Ag@PRV Cable-like NFs. However, the amount of silver loading did not solely determine the antibacterial performance of the materials. MIC/MBC/fluorescence inverted microscopy experiments silver elements on the surface of the materials, the morphology of nano-silver, the contact between nano-silver and bacteria, and the dissolution of silver ions. Notably, the bactericidal effect of the silver-loaded NPs against *E. coli* was more significant than that against *S. aureus* due to the differences in cell membrane/wall structures of Gram-positive and negative bacteria, revealed that Ag@PRV Strawberry-like NPs exhibited the best antibacterial performance. This finding indicated that the antibacterial efficacy was influenced by the distribution of the dense and thicker chitosan cell membrane of Gram-positive bacteria hindered the penetration of nano-silver, resulting in a better barrier effect, and nano-silver could not change the permeability of bacterial cell membrane to kill bacteria in a short time. This study provides insight into the morphological design of nano-silver-modified PRV NPs, explores the application scenarios of different antibacterial active nano-silver-modified PRV NPs, and investigates the antibacterial behavior and mechanism. The results could serve as a foundation for the development of new silver-based antibacterial nanomaterials for different indications.

## Declaration of competing interest

The authors declare that they have no known competing financial interests or personal relationships that could have appeared to influence the work reported in this paper.

## Acknowledgments

This work was financially supported by the Ningbo Scientific and Technological Innovation 2025 Major Project (No. 2020Z097), Natural Science Foundation of Zhejiang Province (No. LY18E030009), Ningbo Clinical Research Center for Otolaryngology Head and Neck Disease (No. 2022L005), and Ningbo Medical and Health Brand Discipline (No. PPXK2018-02).

## Supplementary materials

Supplementary material associated with this article can be found, in the online version, at doi:10.1016/j.cclet.2023.108584.

## References


[1] Z. Qin, Y. Zheng, Y. Wang, et al., Coord. Chem. Rev. 449 (2021) 214218.
[2] S. Chernousova, M. Epple, Angew. Chem. Int. Ed. 52 (2013) 1636–1653.
[3] S. He, J. Liu, S. He, A. Liu, W. Shao, Colloids Surf. A 643 (2022) 128737.
[4] M.G. Mehrabani, R. Karimian, B. Mehramouz, M. Rahimi, H.S. Kafil, Int. J. Biol. Macromol. 114 (2018) 961–971.
[5] X. Liu, K. Gan, H. Liu, et al., Dent. Mater. 33 (2017) e348–e360.
[6] A. Jaggessar, H. Shahali, A. Mathew, P.K. Yarlagadda, J. Nanobiotechnol. 15 (2017) 64.
[7] K. Kapat, Q.T. Shubhra, M. Zhou, S. Leeuwenburgh, Adv. Funct. Mater. 30 (2020) 1909045.
[8] Q. Wu, W.S. Miao, Y.D. Zhang, H.J. Gao, D. Hui, Nanotechnol. Rev. 9 (2020) 259–273.
[9] S.S.D. Kumar, N.K. Rajendran, N.N. Houreld, H. Abrahamse, Int. J. Biol. Macromol. 115 (2018) 165–175.
[10] B.P. Colman, B. Espinasse, C.J. Richardson, et al., Environ. Sci. Technol. 48 (2014) 5229–5236.
[11] M.A. Kakakhel, F. Wu, W. Sajjad, et al., Environ. Sci. Eur. 33 (2021) 1–11.
[12] A.V.A. Mariadoss, K. Saravanakumar, A. Sathiyaseelan, et al., Mater. Today Commun. 35 (2023) 105652.
[13] Y.M. Ge, Y. Zhang, J.S. Yang, et al., Carbohydr. Polym. 312 (2023) 120793.
[14] M. Xu, H. Luo, H. Rong, et al., Int. J. Biol. Macromol. 231 (2023) 123289.
[15] C. Wang, X. Huang, W. Deng, et al., Mater. Sci. Eng. C 41 (2014) 134–141.
[16] X. Chen, X. Huang, C. Zheng, et al., J. Mater. Chem. B 3 (2015) 7020–7029.
[17] H. Huang, L. Mao, Z. Li, et al., J. Bioresour. Bioprod. 4 (2019) 231–241.
[18] E. Nivethaa, S. Dhanavel, A. Rebekah, V. Narayanan, A. Stephen, Mater. Sci. Eng. C 66 (2016) 244–250.
[19] J. Gagnon, M.J. Clift, D. Vanhecke, et al., J. Mater. Chem. B 4 (2016) 1166–1174.
[20] B. Tyliszczak, A. Drabczyk, S. Kudłacik-Kramarczyk, et al., Colloids Surf. B 160 (2017) 325–330.
[21] V. Selin, V. Albright, J.F. Ankner, et al., ACS Appl. Mater. Interfaces 10 (2018) 9756–9764.
[22] A.P. Martinez, B. Qamar, T.R. Fuerst, S. Muro, A.K. Andrianov, Biomacromolecules 18 (2017) 2000–2011.
[23] Z. Li, J. Huang, T. Du, et al., Chin. Chem. Lett. 33 (2022) 2496–2500.
[24] R. Chen, P. Ouyang, L. Su, et al., Chin. Chem. Lett. 33 (2022) 4610–4616.
[25] X. You, L. Wang, J. Zhang, et al., Chin. Chem. Lett. 34 (2023) 107720.
[26] S. Shen, Z. Guo, J. Wang, et al., Mater. Express 11 (2021) 947–958.
[27] C. Wang, W. Tian, Y. Ding, et al., J. Am. Chem. Soc. 132 (2010) 6524–6529.
[28] L. Zhu, Y. Xu, W. Yuan, et al., Adv. Mater. 18 (2006) 2997–3000.
[29] P. Gao, J. Fu, J. Yang, et al., Phys. Chem. Chem. Phys. 11 (2009) 11101–11105.
[30] L. Zhu, Y. Zhu, Y. Pan, et al., Macromol. React. Eng. 1 (2007) 45–52.
[31] J. Fu, Q. Xu, J. Chen, et al., Chem. Commun. 46 (2010) 6563–6565.
[32] X. Wei, H. Chen, H.P. Tham, et al., ACS Appl. Nano Mater. 1 (2018) 3663–3672.
[33] X. Zhao, Y. Wang, J. Li, et al., Anal. Chim. Acta 1160 (2021) 338450.
[34] F.M. Kievit, O. Veiseh, N. Bhattarai, et al., Adv. Funct. Mater. 19 (2009) 2244–2251.
[35] K. Yang, X. Huang, J. He, P. Jiang, Adv. Mater. Interfaces 2 (2015) 1500361.
[36] C. Shuai, G. Liu, Y. Yang, et al., Nano Energy 74 (2020) 104825.
[37] M. Ahmad, T. Nawaz, M.A. Assiri, et al., ACS Omega 7 (2022) 7096–7102.
[38] J. Fu, X. Huang, Y. Huang, et al., J. Phys. Chem. C 112 (2008) 16840–16844.
[39] Z. Miao, D. Yan, T. Zhang, et al., ACS Appl. Mater. Interfaces 13 (2021) 32094–32105.
[40] Y. Xiao, G. Jiang, C. Ma, et al., Chem. Eng. J. 426 (2021) 131839.
[41] C. You, C. Han, X. Wang, et al., Mol. Biol. Rep. 39 (2012) 9193–9201.
[42] N. Durán, M. Durán, M.B. De Jesus, et al., Nanomedicine 12 (2016) 789–799.
[43] S.A. Anuj, H.P. Gajera, D.G. Hirpara, B.A. Golakiya, Eur. J. Pharm. Sci. 127 (2019) 208–216.
[44] N. Dasgupta, C. Ramalingam, Environ. Chem. Lett. 14 (2016) 477–485.
[45] X. Huang, X. Bao, Y. Liu, Z. Wang, Q. Hu, Sci. Rep. 7 (2017) 1860.